
Searching for Moving Objects in HSC-SSP: Pipeline and Preliminary Results

Ying-Tung CHEN¹, Hsing-Wen LIN², Mike ALEXANDERSEN¹, Matthew J. LEHNER^{1,3,4}, Shiang-Yu WANG¹, Jen-Hung WANG¹, Fumi YOSHIDA^{5,6}, Yutaka KOMIYAMA⁷ and Satoshi MIYAZAKI^{7,8}

¹Institute of Astronomy and Astrophysics, Academia Sinica, P. O. Box 23-141, Taipei 106, Taiwan

²Institute of Astronomy, National Central University, 32001, Taiwan

³Department of Physics and Astronomy, University of Pennsylvania, 209 S. 33rd St., Philadelphia, PA 19125, USA

⁴Harvard-Smithsonian Center for Astrophysics, 60 Garden St., Cambridge, MA 02138, USA

⁵Planetary Exploration Research Center, Chiba Institute of Technology, 2-17-1 Tsudanuma, Narashino, Chiba 275-0016, Japan

⁶Department of Planetology, Graduate School of Science, Kobe University, Kobe, 657-8501, Japan

⁷National Astronomical Observatory of Japan, 2-21-1 Osawa, Mitaka, Tokyo 181-8588, Japan

⁸SOKENDAI(The Graduate University for Advanced Studies), Mitaka, Tokyo, 181-8588, Japan

*E-mail: ytchen@asiaa.sinica.edu.tw

Received ; Accepted

Abstract

The Hyper Suprime-Cam Subaru Strategic Program (HSC-SSP) is currently the deepest wide-field survey in progress. The 8.2 m aperture of Subaru telescope is very powerful in detecting faint/small moving objects, including near-Earth objects, asteroids, centaurs and Trans-Neptunian objects (TNOs). However, the cadence and dithering pattern of the HSC-SSP are not designed for detecting moving objects, making it difficult to do so systematically. In this paper, we introduce a new pipeline for detecting moving objects (specifically TNOs) in a

non-dedicated survey. The HSC-SSP catalogs are re-arranged into the HEALPix architecture. Then, the stationary detections and false positive are removed with a machine learning algorithm to produce a list of moving object candidates. An orbit linking algorithm and visual inspections are executed to generate the final list of detected TNOs. The preliminary results of a search for TNOs using this new pipeline on data from the first HSC-SSP data release (Mar 2014 to Nov 2015) are also presented.

Key words: Kuiper belt: general — Minor planets, asteroids: general — Methods: data analysis

1 Introduction

Minor planets are the proxy to understand the history and evolution of the Solar System. In the past two decades, several surveys have used different facilities to discover near-Earth asteroids (NEAs), main belt asteroids (MBAs), Centaurs and trans-Neptunian Objects (TNOs). For the nearby objects (NEAs, MBAs), small telescopes with quick response times are very efficient at detecting them and are thus useful to help understand the population of Earth’s neighborhood. For more distant objects (Centaurs, TNOs), large telescopes are used to gather more photons from objects with less reflecting light (Elliot et al. 2005; Kaiser et al. 2010; Petit et al. 2011; Alexandersen et al. 2016; Bannister et al. 2016). Due to the difficulty of obtaining accurate data on small objects at such large distances, the physical properties of only the brightest, largest objects have been well studied. However, the fainter, smaller objects can provide important clues to understand the collisional and accretion processes in the evolution of the Solar System. Recent spacecraft missions, including the Rosetta mission to the comet 67P/ChuryumovGerasimenko (Fornasier et al. 2015) and the Hayabusa mission to 25143 Itokawa (Fujiwara et al. 2006) reveal that our understanding of small Solar System objects is quite limited.

The Hyper Suprime-Cam Subaru Strategic Program (HSC-SSP) is a large program on the 8.2 m Subaru telescope, using the large 1.7 deg^2 field-of-view (FoV) camera, HSC, to survey around 1400 deg^2 of the sky. The uniqueness of this facility makes HSC-SSP the deepest wide-field survey currently in operation. Having started in 2014, HSC-SSP will use 300 Subaru telescope nights over 6 years (2014-2019).

The cadence of a wide-field survey is very crucial to efficiently detect moving objects. For a dedicated survey of TNOs, the survey cadence usually requires a pair or a triplet of exposures with one to a few hours separation and the same pointing to discover the objects. The Deep Ecliptic Survey (DES) was one of the first wide-field surveys focused on the outer Solar System objects (Elliot et al. 2005). After that, the Canada-France Ecliptic Plane Survey (CFEPS) was the first dedicated survey with a full characterization including orbital parameter determination and detection efficiencies (Petit et al. 2004; Kavelaars et al. 2009; Petit et al. 2011). CFEPS used a set of three exposures ($\sim 1 \text{ hr}$ cadence) to resolve the motions of TNOs. Following CFEPS, the Panoramic Survey Telescope and Rapid Response System 1 (Pan-STARRS 1, or PS1) project searched for Solar System objects in a 3π area of the sky. The major goals of PS1 were to detect NEAs (Wainscoat et al. 2014) and TNOs (Chen et al. 2016; Lin et al. 2016) with a sub-hour cadence. In the above projects, a specific pipeline was designed to operate with the preferred cadence. The PS1 moving objects pipeline, the Moving Object Processing System (MOPS, Denneau et al. 2013), was applied to detect asteroids and NEAs, while

the PS1 Outer Solar System (OSS) team developed a different pipeline to detect TNOs (Holman et al. 2015).

The major goal of HSC-SSP is to address outstanding astrophysical questions such as the nature of dark matter and dark energy, the cosmic re-ionization, and galaxy evolution over cosmic timescales. In this survey, a wide-dithering pattern with sub-hour cadence under similar weather condition is often applied to fill up the gaps between CCDs of HSC in order to obtain complete coverage of a targeted field. Such a survey strategy makes it extremely difficult to detect moving objects using the conventional techniques used by the TNO surveys described above. Also, the high number density of the detections in HSC image results in unreasonable requirements for CPU time if the pipeline uses the extensively adopted KD-Tree (Bentley 1975; Kubica et al. 2005) algorithm. However, we would like to utilize the data set from the HSC survey to search for small TNOs. Finding more faint TNOs is essential to determine the faint end of the TNO size distribution, and the wide field and depth of HSC-SSP has a unique potential to find a large number of such objects.

In order to search for TNOs in this data set, we thus needed to develop a new moving object pipeline, HSC-MOP, to detect Solar System objects in the HSC-SSP data. The pipeline is capable of detecting the moving objects in a wide-field survey with a non-uniform dithering cadence like that of the HSC-SSP. This pipeline has the ability to detect moving objects in images with different time separations and different limiting magnitudes.

The rest of this paper is organized as follows. In section 2, we introduce the first data release of the HSC-SSP, which includes observations taken from 2014 to 2015 (Aihara et al. 2017). In section 3, we describe our moving object pipeline. In section 4, we present the preliminary results of a search for TNOs using our pipeline on the first HSC-SSP data release. Finally, in section 5, we conclude the paper with a summary of our results.

2 Data status

The HSC-SSP survey is executed with HSC which consists of 116 2048 x 4176 pixel CCDs, with a pixel scale of $0.168''$. (Miyazaki et al. 2012). 104 of the CCDs are for science. With a 1.76 deg^2 FoV, HSC-SSP will survey $\sim 1400 \text{ deg}^2$ using Sloan-like g , r , i , z , and y broadband filters. The first data set was released on 27 February 2017¹ (Aihara et al. 2017).

There are three layers of the HSC-SSP survey including WIDE, DEEP, and UDEEP fields, each with different coverage areas and limiting magnitudes. We only process the WIDE layer of data in this study to maximize the FoV for the search of TNOs. Note that the first data release of HSC-SSP

¹ <http://hsc.mtk.nao.ac.jp/ssp/>

only include the sky regions covered in all the five filters, which is different from what we analysed in this study – we did not require the fields to be imaged in z or y bands. The HSC-SSP observations are acquired in patches, each patch covering a sky area formed by a dithered layout of the 1.7 deg^2 HSC FoV, such that the gaps between CCD chips could be covered and the survey area would have the required exposure depth for the primary science goals.

Because the weather conditions and schedule arrangements vary in each run, the HSC-SSP has a flexible schedule for the sequence of observations. As a result, the patches observed with each filter in a single dark run have different sizes. In this study, we analyzed the images with deepest limiting magnitudes i.e. ~ 3 minute exposures taken in HSC- g , HSC- r , HSC- i , HSC- $r2$, and HSC- $i2$ filters. The calibration images using shorter exposure time (~ 30 second) are not included in this study. The limiting magnitude of each HSC- r exposure is around 25.0 to 25.5 mag. Note that the original r - and i -band filters of HSC (HSC- r and HSC- i) were replaced with new ones (HSC- $r2$ and HSC- $i2$) in June 2016 and Nov 2015, respectively. The transmission curve for the old filters and the new ones are similar, but the new HSC- $r2$ and HSC- $i2$ filters have more uniform transparency than HSC- r and HSC- i across the effective area. There is no data using new filters in this study.

The solar elongation is a crucial celestial parameter for observing Solar System objects. Due to phase effects, objects are fainter as their locations farther from opposition. Furthermore, for objects observed at opposition ($\sim 180^\circ$ solar elongation angle), the parallax from the motion of the Earth dominates the apparent motion of objects across the sky (except for NEAs), such that the rate of apparent motion is strongly dependent on the distance of the objects. The actual motion of the objects only provides substantial contributions to the apparent motion once the solar elongation is $< 140^\circ$ or $> 220^\circ$ ($> 40^\circ$ from opposition). The rates of motion of asteroids and TNOs are thus occasionally identical when the observations are far from opposition, causing confusion (see Figure 1). Because the HSC-SSP is not a dedicated survey for Solar System science, many observations are acquired far from opposition. To avoid possible confusion of our detections, we limit our search to only data taken within ± 40 degrees from opposition (see Figure 2). With this limit, $\sim 221 \text{ deg}^2$ out of the 333.5 deg^2 survey area taken from March 2014 to November 2015 was used for this study (see Figure 3 and Table 1).

3 Pipeline

This section contains details about each step of our moving object detection pipeline - HSC-MOP. We begin with a quick overview, followed by detailed explanations of each step.

3.1 Overview

Our data process starts from the reduction of raw images with `hscPipe`, the official HSC-SSP pipeline (Bosch et al. 2017, in prep). A catalog of detected sources is created for each exposure generated from `hscPipe`. Each field is then divided into different sky regions using HEALPix (Górski et al. 2005). The catalogs for each exposure which overlap each HEALPix region are combined in to a master catalog. Objects which appear at the same place in multiple exposures are entered into a stationary catalog. A combination of machine learning algorithm and `hscPipe` flags are then used to find candidate non-stationary (that is, moving) sources. After we build catalogs of non-stationary sources, a linear search algorithm is applied to identify possible moving objects. Such candidates would appear as non-stationary objects in different exposures with offset positions consistent with a moving object. These candidates are then verified with Initial Orbit Determination (IOD, see Bernstein & Khushalani 2000) to generate the list of possible candidates. Finally, all candidates are checked by visual inspection, using the Zooniverse platform. The Figure 4 shows a flowchart of this pipeline.

3.2 `hscPipe`

`hscPipe` is the official pipeline to process data obtained from HSC, and is maintained by the HSC-SSP team. The standard outputs from `hscPipe` include a fits table catalog and calibrated images (debiased, flat-fielded). `hscPipe` uses the internal Pan-STARRS 1 catalog (*ps1_pv2*) to calibrate astrometry and photometry (Schlafly et al. 2012; Tonry et al. 2012; Magnier et al. 2013). The average astrometric scatter in an individual chip image is smaller than 30 milliarcsec. It should be noticed that the current version of `hscPipe` still has some limitations on processing CCD chips containing very bright stars.

3.3 HEALPix

To handle the dithering observations, we adopted the Hierarchical Equal Area isoLatitude Pixelation of a sphere (HEALPix) (Górski et al. 2005) to manage the catalogs acquired in a dark run. The HEALPix is an algorithm to produce a subdivision of the all sky, each pixel covers the same surface area as every other pixel. We adopt $n_{\text{side}} = 32$ (12288 pixels for all sky) in the pipeline to build a set of reasonably sized sky regions so that the pipeline can detect slower-moving objects within the same HEALPix. The mean size for each HEALPix is 1.8323 deg (equals to 3.36 deg^2 , see Figure 5) to match the HSC FoV. Every detection catalog is separated and saved according to the corresponding HEALPix.

3.4 stationary catalog

Most of the sources in the sky are stationary sources, i.e. background stars and galaxies. Detections of stationary sources should be at identical locations in different exposures, no matter when the images were taken. However, depending on the search criteria, moving objects might be cataloged as stationary objects. For example, objects beyond 50 au could be confused for stationary sources if the time-span between the images is not long enough for the object to move noticeably. To avoid possible removal of the moving objects beyond the Kuiper Belt, we define a stationary object as (1) detected in at least two images within a radius of $0.5''$, and (2) with the separation between the image epochs longer than 20 minutes. We use $0.5''$ instead of a larger radius after considering the HSC-SSP cadence, the false positive rate and the average seeing conditions of the data. Due to the cadence limitation of SSP, we could not choose a shorter maximum separation of the matched detection epochs. Under such conditions, only objects located at opposition and further than 100 au might erroneously be labeled as stationary objects. All exposures in each dark run are used to generate the stationary catalog, which is then applied in the next step which to remove the stationary detections and false positives.

3.5 Machine learning to remove false positive

After removing the stationary sources, there are still ~ 0.5 million unclassified source detections in each HEALPix region. In addition to the real moving objects and transient events, the unclassified detections also include some stars and galaxies with bad centroids and other possible artifacts. Therefore, processing all such detections without any further reductions will significantly impact the performance and speed of the moving object detection pipeline. To conquer this problem, we adapted a machine learning (ML) based real-bogus system and hscPipe flags to pick-up real astronomical detections and to reject the false positives. This system separates the real non-stationary sources and false positives by using 49 parameters generated from the hscPipe. These parameters mostly comprise the various photometric measurements (flux and error) and shape moments. Details of the 49 parameters are presented in Lin et al. (2017, submitted).

Our real-bogus system can reach a true positive rate (tpr) of $\sim 96\%$ with a false positive rate (fpr) of $\sim 1\%$, tpr $\sim 99\%$ with fpr $\sim 5\%$, or tpr $\sim 99.5\%$ with fpr $\sim 15\%$. We found that with the 1% fpr threshold, the system can reduce the number of unclassified detections by half. If we relax the threshold to 15% fpr, it can still reduce the number of unclassified detections by one third. After several tests, we found that the pipeline could handle the remaining two thirds of the detections. We therefore set the threshold of fpr at 15% so that 99.5% of the real detections get passed, while $\sim 85\%$ of the original false detections get removed. For example, there are ~ 0.5 million non-stationary

detections in the HEALPix for one SSP observation run without any false-positive cut. With the real-bogus system, $\sim 160,000$ potentially false detections are rejected. The remaining sources are dominated by the faint real astronomical sources (stars, galaxies and etc). Since the detectability of very faint objects is highly sensitive to image quality (e.g., seeing and transparency), some of them cannot be removed by the stationary selection criteria. For details of the real-bogus system, we refer the reader to Lin et al. (2017, submitted).

3.6 grid linear search

The next step of the pipeline is to search for matched detections of a candidate moving object in a single night. To maximize the number of candidates, we developed a new algorithm to detect possible moving objects, with the following steps.

First, all non-stationary catalogs are merged into a single fits table, which includes the time, zero-point and image file path. The zero-point is used for calculating magnitude, while the image file path is for making postage stamp images to be used in the following step (see section 3.9). We use the Python module Numpy to generate the catalogs.

Second, we use a simple Monte Carlo simulation to obtain the mean direction of motion of TNOs on the sky region at the time of the dark run. Then the linear search scans the full area of a HEALPix region within a range of $\pm 30^\circ$ of the resulting mean direction of motion. Detections located within $2''$ of a line along a given direction of motion are grouped as a subset, which will be verified if any reasonable group exists. This is demonstrated in Figure 6.

With the grouped detections (sorted by RA), reasonable tracks (that is, groups of source detections spanning multiple images consistent with moving objects) are then identified using the following conditions: (1) correct time order along the line, (2) rates of motion $< 49''/\text{hr}$ (ranging from asteroids to TNOs), (3) $\Delta\text{mag} < 2.0$ across the different images, and (4) more than 3 detections. After the selection, the tracks of the candidates of moving objects are saved into a database.

3.7 linking

After we get a track of a candidate object in images taken over a single night, we link tracks from different nights that might belong to the same object. The criteria are set by (1) similar rate and direction of motion, (2) source positions across the multiple images consistent with a reasonable orbit. If the combination of two tracks satisfies the above criteria, the joined tracks are then examined by IOD (Bernstein & Khushalani 2000), which provides estimates of the orbital parameters, in particular semi-major axis a and inclination i . If all residuals of the fit are smaller than $0.3''$, we regard the

object as a candidate.

3.8 Collection of similar candidates

The linking procedure can eliminate most of the false combinations. However, it is still possible that one track in a night can still link to two different tracks in the other night and produce two valid candidates. It is difficult to distinguish the correct link from the false links without any visual inspection. Therefore, we collect the similar candidates (the candidates that share part of their tracks). These candidates are then visually inspected.

3.9 Visual Inspection

Visual inspection is frequently used to check whether moving object candidates are real objects or false positives. The pipeline generates postage stamp images (fits and png) for each candidate, which are centered in the postage stamp images (see Figure 7). We only inspect objects with $a > 20$ au (from the IOD orbit fit) in order to avoid including asteroids. A set of six truncated images (three images are from day one, three images are from day two) is uploaded to the Zooniverse platform for the inspection by team members. Zooniverse is a citizen science interface, which is used by many scientific projects, including astronomy and ecology (Trouille et al. 2017). The Zooniverse project builder provides a very simple interface to launch a visual inspection project with no required understanding the backbone structure. Because of the HSC-SSP data policy, we built the visual inspection page as a private project. Every candidate which is validated by at least two team members is listed as a real object.

3.10 Process Note

This pipeline simply searches the candidates moving within a single HEALPix region. The current goal of this pipeline is to discover moving objects that move at a rate slow enough to keep most of them in the same HEALPix region within one observational run. The detection of objects that cross from one HEALPix region to another will be future work for finding asteroids or other nearby objects.

4 Preliminary Results and Discussion

We applied this pipeline to the HSC-SSP data taken from March 2014 to November 2015. Around two thousand moving-objects candidates in each dark run were detected, including asteroids, centaurs, and TNOs. In this paper, we only present the results of our TNO search, so only the objects with semi-major axes larger than 20 au were selected for visual inspection. More than 500 candidates (including

false positives) meet this criterion. A total of 231 of these TNO candidates pass visual inspection by at least two members (see Table 2). Although the HSC-SSP had nine dark runs in first data release, we only analyzed the dark runs with solar elongations in our required range, and which also have a sufficient number of exposures for the detection pipeline to function. These are images taken in 2014/11, 2015/03, 2015/05 and 2015/10 runs (See Table 1).

4.1 Detection Efficiency

To understand the survey depth and the detection efficiency (both as a function of object brightness and moving rate) of the HSC-SSP, we generated synthetic moving objects with a magnitude range of 22 - 26 and a rate of motion of $1''$ – $15''$ /hr (emulating objects at 10-100 au at opposition). Each chip has around 100 synthetic objects added. The PSFs of the synthetic moving objects are generated using a 2D Gaussian function with the FWHM equal to the mean seeing. The raw images were implanted with the synthetic moving objects, and were then processed by `hscPipe` in the same way as the regular data processing to inspect the net efficiency of the detection pipeline. The result is shown in Figure 8. The efficiency as a function of magnitude was fit with a detection efficiency function in Alexandersen et al. (2016) and Bannister et al. (2016) as follows:

$$\eta(m_r) = \eta_0 - c(m_r - 22)^2 \left[1 + \exp\left(\frac{m_r - m_L}{w}\right) \right]^{-1} \quad (1)$$

This function gives an efficiency of about η_0 at $m_r = 22$, and it decreases quadratically with magnitude until it drops more steeply near the magnitude limit m_L with an exponential falloff width w . The efficiency of HSC-SSP is best represented with $\eta_0 = 0.38$, $c = 0.015$, $m_L = 25.41$ and $w = 0.033$. Considering that the TNO detection criteria of our pipeline require at least three individual detections on two different nights (six in total), the maximum detection efficiency below 40% is expected. Given at least six exposures and the $\sim 85\%$ to 90% fill factor in a single HSC exposure, the net efficiency will be $0.85^6 \sim 0.38$ to $0.9^6 \sim 0.53$ for detecting the moving objects.

4.2 Orbit

As discussed above, the orbital parameters and uncertainties of each candidate are calculated using the Bernstein & Khushalani (2000) routine. The orbital uncertainties of these candidates are not negligible because the observations generally span less than a month. Due to the short arc of these observations, the predicted on-sky position uncertainty grows quickly, making the objects difficult to follow-up after the semester of discovery. We then tested Bernstein & Khushalani (2000) routine using known TNOs with a cadence similar to HSC-SSP, the results show that the orbital inclination is the only reliable orbital parameter for a TNO with short-arc observations. We are thus able to

separate the sample (Volk & Malhotra 2011) into a cold population ($i + \sigma_i < 5^\circ$) and a hot population ($i - \sigma_i > 5^\circ$). After this process we find a total of 164 hot objects in our list of TNOs. This simple cut means there will be a minor contamination of hot objects in the cold population, but our hot population is useful for qualitative analysis.

4.3 Absolute Magnitude Distribution

Although the orbital uncertainties of these candidates don't allow dynamical classification, flux corrections are still achievable. The absolute magnitude H of each candidate can be calculated using the photometry and initial orbital solutions. Even though the short arcs of these candidates produce uncertainties of around 2 au in the barycentric distance by Bernstein & Khushalani (2000), our results are comparable with Fraser et al. (2014). These preliminary results have not yet been debiased with the detection efficiencies, so we only consider the bright candidates with $H_r < 7.7$. In Figure 9, the best fit slope of a single power law to the absolute magnitude distribution of hot objects with $H_r < 7.7$ is 0.77. This value is consistent with the results from Fraser et al. (2014), which has a slope of $0.87^{+0.07}_{-0.2}$ before the break magnitude at $H_r = 7.7$.

4.4 Color Distribution

The bimodal color distribution of outer Solar System objects has been known for a decade (Peixinho et al. 2003; Barucci et al. 2005; Perna et al. 2010; Peixinho et al. 2012; Lacerda et al. 2014). This bimodal color distribution implies that different evolution processes or surface compositions may occur in the early history of the outer Solar System. While the selected targets in the literature include the observational biases, resulting in non-uniform samples, recent research using the Subaru HSC resulted in a robust bimodal color distribution of small objects in the hot population (Wong & Brown (2017), Figure 3). The $g - i$ color distribution of our sample is compatible with these results. Although the rotation effects and observational biases have not removed from our results, the photometry from using two filters in different nights could still provide an approximate color properties of the TNO surfaces.

As mentioned in above, the HSC-SSP is not optimized for Solar System science, and this is reflected in the choice of filters for different observations as well as the survey cadence. Measurements of $g - r$ colors of 116 hot TNOs indicate a peak of count number at 0.6 (See Figure 10). Measurements of $g - i$ colors of only 24 hot TNOs are available in the first data release (images taken between March and May 2015). In Figure 10, a sharp bluer peak at $g - i = 0.9$ is consistent with the bluer peak ($g - i = 0.91$) of the bimodal color distribution in Wong & Brown (2017). Unfortunately, the sample

of redder TNOs ($g - i > 1.0$) we found with the HSC-SSP is currently too small to compare with the redder peak at $g - i = 1.42$ reported by Wong & Brown (2017). With additional discoveries of TNOs beyond the first HSC-SSP data release, a larger database of the hot TNO $g - i$ colors will be available to examine the bimodal color distribution and further explore the surface properties of these objects.

4.5 Existence of vertical Centaur/TNO Belt?

The recent discovery of a possible common plane in giant planet region provides evidence of the existence of a high-inclination ($60^\circ < i < 120^\circ$) and high-perihelion ($q > 10$ AU) belt (Chen et al. 2016). The clustering of ascending nodes is the significant feature of this common plane. To farther confirm the existence of the vertical plane, the total numbers of high-inclination Centaurs/TNOs need to be increased for improving the significant in statistics. The surface density of high-inclination Centaurs/TNOs “on” and “off” this common plane is a probe of intrinsic population. Although the survey fields of entire HSC-SSP almost have no overlapping region with proposed sky region of this belt (See Figure 3 in this study and Figure 4 in Chen et al. (2016)), the HSC-SSP could provide the “off” plane observations as a control samples to examine this hypothesis.

In our candidates, the highest inclination of prograde objects is 53° ; none of the eight retrograde objects are in this vertical plane ($60^\circ < i < 120^\circ$). For a sanity check, we used another orbital fitting code, `OpenOrb` (Granvik et al. 2009), to validate the inclinations of the retrograde objects. The results show that two of the eight retrograde objects are possibly main-belt asteroids with low inclinations, and the other six have the orbital solutions with the inclination near $\sim 30^\circ$ or $\sim 130^\circ$. Although both orbit fitting codes show the very low possibility that these eight retrograde objects are orbiting in this vertical plane, additional follow-up observations definitely will provide a robust inclination solution.

The result of a non-detection of high-inclination TNOs in this vertical plane corresponds a low column density of “off” plane objects. However, for getting a relevant upper limit, the combination of the HSC-SSP results, follow-up observations and future on-common plane observations using also the HSC will provide a statistically valid test of the existence of this vertical Centaur/TNO Belt.

4.6 Asteroids

This pipeline has the ability to find the asteroid tracks in a single night, and thousands of asteroids were detected in this data set. However, the orbital fitting code we used was designed for identifying TNOs, and the orbit fitting for asteroids is not robust. We will use an alternative code for asteroids in a future analysis.

5 Summary

The HSC-SSP is currently the deepest ongoing survey, and will cover more than 1400 deg². This data set provides an excellent opportunity to explore various topics in observational astronomy. In this study, we have described in detail the main algorithms of our moving object pipeline, which could be used in a survey with dithering pointings, e.g. HSC-SSP. This search algorithm could provide a better approach to discover Solar System objects in the future large surveys, which have non-optimal cadences or dithered pointings. Compared with other moving object pipelines for searching for TNOs, this pipeline has fewer limitations on survey cadence and pointing, which are very critical parameters for the detection of moving objects. The false positive rate of single detections in the catalog was significantly reduced to 15% with our ML algorithms. The ML also indirectly decreases the false positive rate of moving object candidates. We used the pipeline we have developed to examine the first data release of the HSC-SSP (2014-2015).

The preliminary search of this first data set has yielded 231 TNOs candidates that pass our search criteria. The lack of follow-up observations leads to large uncertainties in orbital parameters except for inclination. The absolute magnitude distribution of HSC-SSP TNOs shows a slope of 0.77 which is shallower than a recently study of 1.45 (Wong & Brown 2017), but our value is consistent with the study with proper calibrations (Fraser et al. (2014), $\alpha = 0.87^{+0.07}_{-0.2}$). The $g-i$ color distribution of HSC-SSP hot TNOs agrees with the bluer peak of bimodal distribution mentioned in the recent study. More detections in future HSC-SSP data sets will provide a significant number of detections of faint TNOs which can be used to improve our understanding of the formation history of the Solar System.

Acknowledgments

We are grateful to Yi-Ching Chiu, Paul Price and Hisanori Furusawa for kindly suggestions and helps in data process. This work was supported in part by MOST Grant: MOST 104-2119-008-024 (TANGO II) and MOE under the Aim for Top University Program NCU, and Macau Technical Fund: 017/2014/A1 and 039/2013/A2. HWL acknowledges the support of the CAS Fellowship for Taiwan-Youth-Visiting-Scholars under the grant no. 2015TW2JB0001. This publication uses data generated via the Zooniverse.org platform, development of is which funded by generous support, including a Global Impact Award from Google, and by a grant from the Alfred P. Sloan Foundation. The Hyper Suprime-Cam (HSC) collaboration includes the astronomical communities of Japan and Taiwan, and Princeton University. The HSC instrumentation and software were developed by the National Astronomical Observatory of Japan (NAOJ), the Kavli Institute for the Physics and Mathematics of the Universe (Kavli IPMU), the University of Tokyo, the High Energy Accelerator Research Organization (KEK), the Academia Sinica Institute for Astronomy and Astrophysics in Taiwan (ASIAA), and Princeton University. Funding was contributed by the FIRST program from Japanese Cabinet Office, the Ministry of Education, Culture, Sports, Science and Technology (MEXT), the Japan Society for the Promotion of Science (JSPS), Japan Science and Technology Agency (JST), the Toray Science Foundation, NAOJ, Kavli IPMU, KEK, ASIAA, and Princeton University.

This paper makes use of software developed for the Large Synoptic Survey Telescope. We thank the LSST Project for making their code

available as free software at <http://dm.lsst.org>

The Pan-STARRS1 Surveys (PS1) have been made possible through contributions of the Institute for Astronomy, the University of Hawaii, the Pan-STARRS Project Office, the Max-Planck Society and its participating institutes, the Max Planck Institute for Astronomy, Heidelberg and the Max Planck Institute for Extraterrestrial Physics, Garching, The Johns Hopkins University, Durham University, the University of Edinburgh, Queens University Belfast, the Harvard-Smithsonian Center for Astrophysics, the Las Cumbres Observatory Global Telescope Network Incorporated, the National Central University of Taiwan, the Space Telescope Science Institute, the National Aeronautics and Space Administration under Grant No. NNX08AR22G issued through the Planetary Science Division of the NASA Science Mission Directorate, the National Science Foundation under Grant No. AST-1238877, the University of Maryland, and Eotvos Lorand University (ELTE) and the Los Alamos National Laboratory.

Based on data collected at the Subaru Telescope and retrieved from the HSC data archive system, which is operated by Subaru Telescope and Astronomy Data Center, National Astronomical Observatory of Japan.

References

- Aihara, H., Armstrong, R., Bickerton, S., et al. 2017, arXiv:1702.08449
- Alexandersen, M., Gladman, B., Kavelaars, J.J., et al. 2016, AJ, 152, 111
- Bannister, M. T., Kavelaars, J. J., Petit, J.-M., et al. 2016, AJ, 152, 70
- Barucci, M. A., Belskaya, I. N., Fulchignoni, M., & Birlan, M. 2005, AJ, 130, 1291
- Bentley, J. 1975, Comm. of the ACM, 18, 9
- Bernstein, G., & Khushalani, B. 2000, AJ, 120, 3323
- Bosh et al. 2017 PASJ, in prepare
- Chen, Y.-T., Lin, H. W., Holman, M. J., et al. 2016, ApJL, 827, L24
- Denneau, L., Jedicke, R., Grav, T., et al. 2013, PASP, 125, 357
- Elliot, J. L., Kern, S. D., Clancy, K. B., et al. 2005, AJ, 129, 1117
- Fornasier, S., Hasselmann, P. H., Barucci, M. A., et al. 2015, A&A, 583, A30
- Fraser, W. C., Brown, M. E., Morbidelli, A., Parker, A., & Batygin, K. 2014, ApJ, 782, 100
- Fujiwara, A., Kawaguchi, J., Yeomans, D. K., et al. 2006, Science, 312, 1330
- Granvik, M., Virtanen, J., Oszkiewicz, D., & Muinonen, K. 2009, Meteoritics and Planetary Science, 44, 1853
- Górski, K. M., Hivon, E., Banday, A. J., et al. 2005, ApJ, 622, 759
- Holman, M. J., Chen, Y.-T., Lin, H.-W., et al. 2015, AAS/Division for Planetary Sciences Meeting Abstracts, 47, 211.12
- Kaiser, N., Burgett, W., Chambers, K., et al. 2010, Proc. SPIE, 7733, 77330E
- Kavelaars, J. J., Jones, R. L., Gladman, B. J., et al. 2009, AJ, 137, 4917
- Kubica, J., Moore, A., Connolly, A., & Jedicke, R. 2005, Proc. SPIE, 5913, 242
- Lacerda, P., Fornasier, S., Lellouch, E., et al. 2014, ApJL, 793, L2
- Lin, H. W., Chen, Y.-T., Holman, M. J., et al. 2016, AJ, 152, 147

Lin et al. 2017 PASJ, submitted

Magnier, E. A., Schlafly, E., Finkbeiner, D., et al. 2013, ApJS, 205, 20

Miyazaki, S., Komiyama, Y., Nakaya, H., et al. 2012, Proc. SPIE, 8446, 84460Z

Peixinho, N., Doressoundiram, A., Delsanti, A., et al. 2003, A&A, 410, L29

Peixinho, N., Delsanti, A., Guilbert-Lepoutre, A., Gafeira, R., & Lacerda, P. 2012, A&A, 546, A86

Perna, D., Barucci, M. A., Fornasier, S., et al. 2010, A&A, 510, A53

Petit, J.-M., Holman, M., Scholl, H., Kavelaars, J., & Gladman, B. 2004, MNRAS, 347, 471

Petit, J.-M., Holman, M. J., Gladman, B. J., et al. 2006, MNRAS, 365, 429

Petit, J.-M., Kavelaars, J. J., Gladman, B. J., et al. 2011, AJ, 142, 131

Schlafly, E. F., Finkbeiner, D. P., Jurić, M., et al. 2012, ApJ, 756, 158

Tonry, J. L., Stubbs, C. W., Lykke, K. R., et al. 2012, ApJ, 750, 99

Trouille, L., Lintott, C., Miller, G. & Spiers, H. 2017, MW17: MW 2017

Volk, K., & Malhotra, R. 2011, ApJ, 736, 11

Wainscoat, R., Veres, P., Bolin, B., et al. 2014, Asteroids, Comets, Meteors 2014,

Wong, I., & Brown, M. E. 2017, AJ, 153, 145

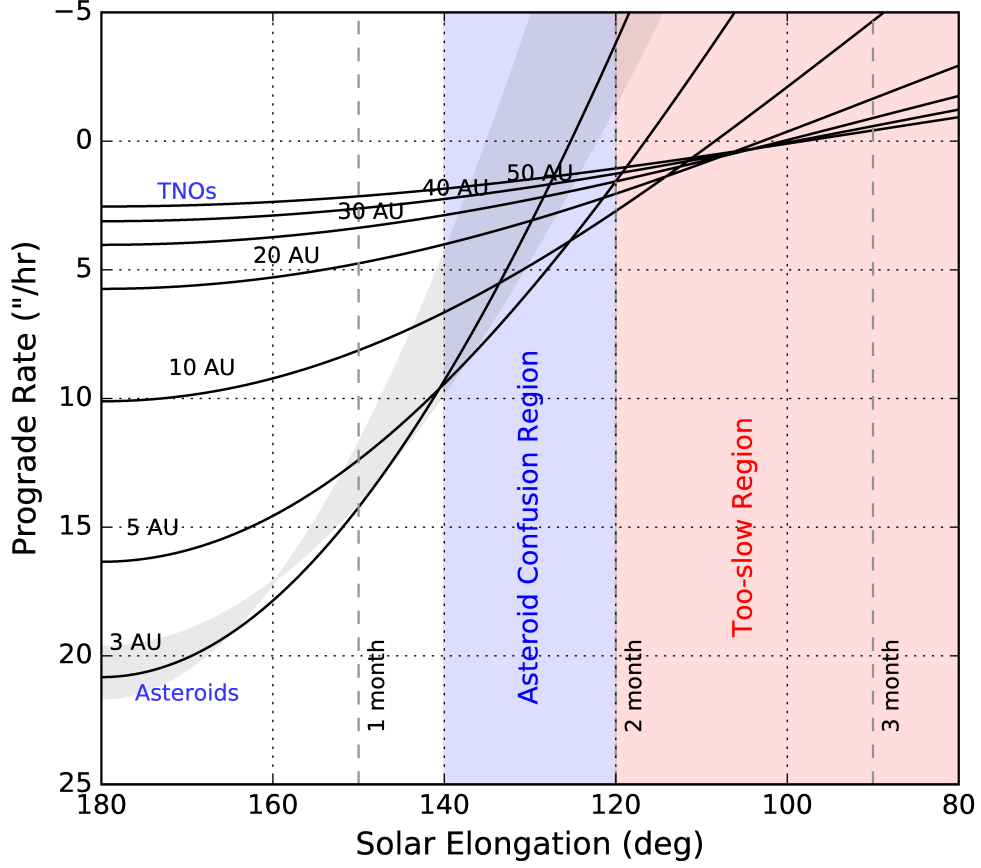


Fig. 1. Rate of motion versus solar elongation angle. The vertical dashed lines show the solar elongation angles corresponding to the time to opposition. The blue rectangle indicates that the TNOs and asteroids have similar rates of motion. The gray region indicates the rates of motion for main belt asteroids.

Table 1. The target regions in the first data release of HSC-SSP used in the moving object search.

Observation Date	R.A.	Decl.	Ec. lat.	Effective Area	Filter	Number of Candidates
	(deg)	(deg)	(deg)	deg ²		
2014/11	34.5	-5.4	-18.1	38.5	g, r, i	8
2015/03	180.2	0.1	0.2	29.7	g, r, i	92
2015/03	217.3	0.2	14.1	24.6	g, r, i	9
2015/05	218.5	-1.2	13.2	29.3	g, r, i	28
2015/05	245.5	43.1	63.0	11.1	g, r, i	0
2015/10	27.7	-1.1	-11.7	79.2	g, r	93
2015/10	340.4	0.5	8.1	8.6	g, r	1

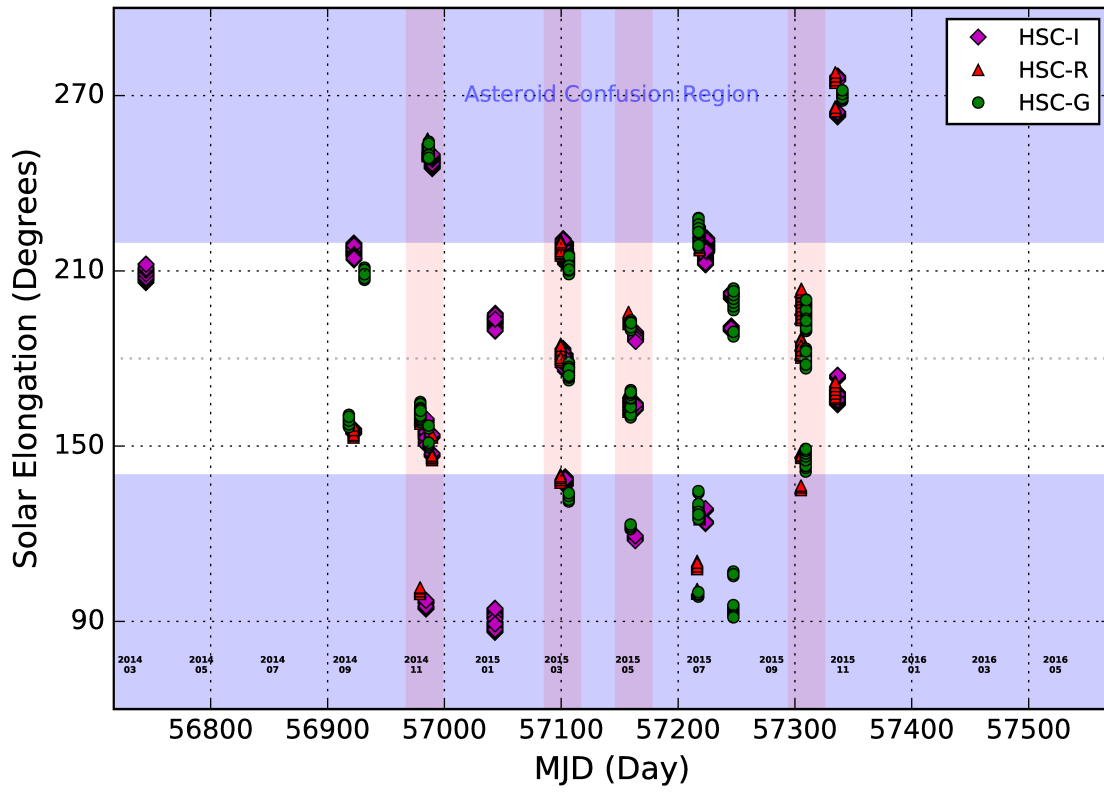


Fig. 2. The solar elongations of HSC fields for images taken 2014–2015. The red regions indicate the dark runs with enough exposures for data analysis, and the blue regions are excluded from this analysis due to the large solar elongations.

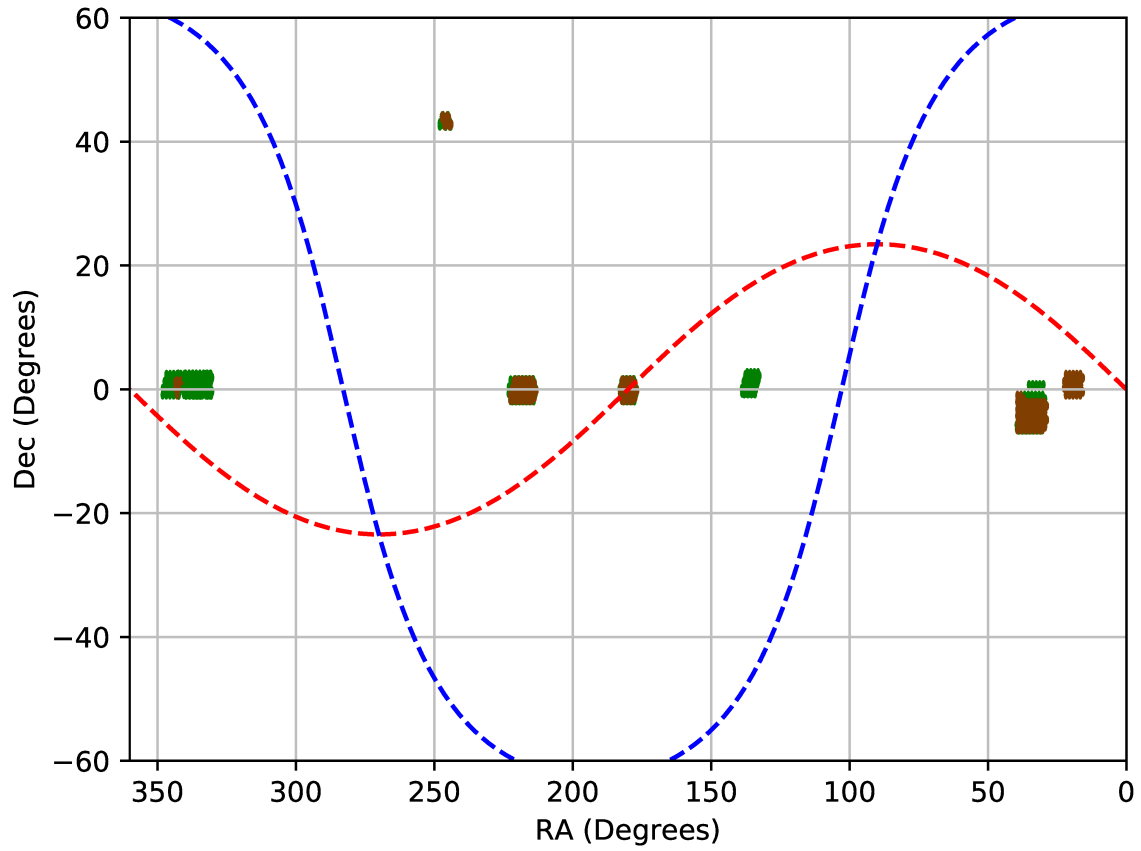


Fig. 3. The HSC-SSP survey fields used in this analysis. Only g , r , and i exposures within ± 40 degree to opposition in the first data release were considered. The ecliptic plane and galactic plane are showed with dashed lines in red and blue. The green regions indicate the total area of all FoVs using g , r , i filters. The brown regions show the areas used in our moving object search. Note the sky regions is different from the first data release of HSC, which only include the area covered in all the five filters.

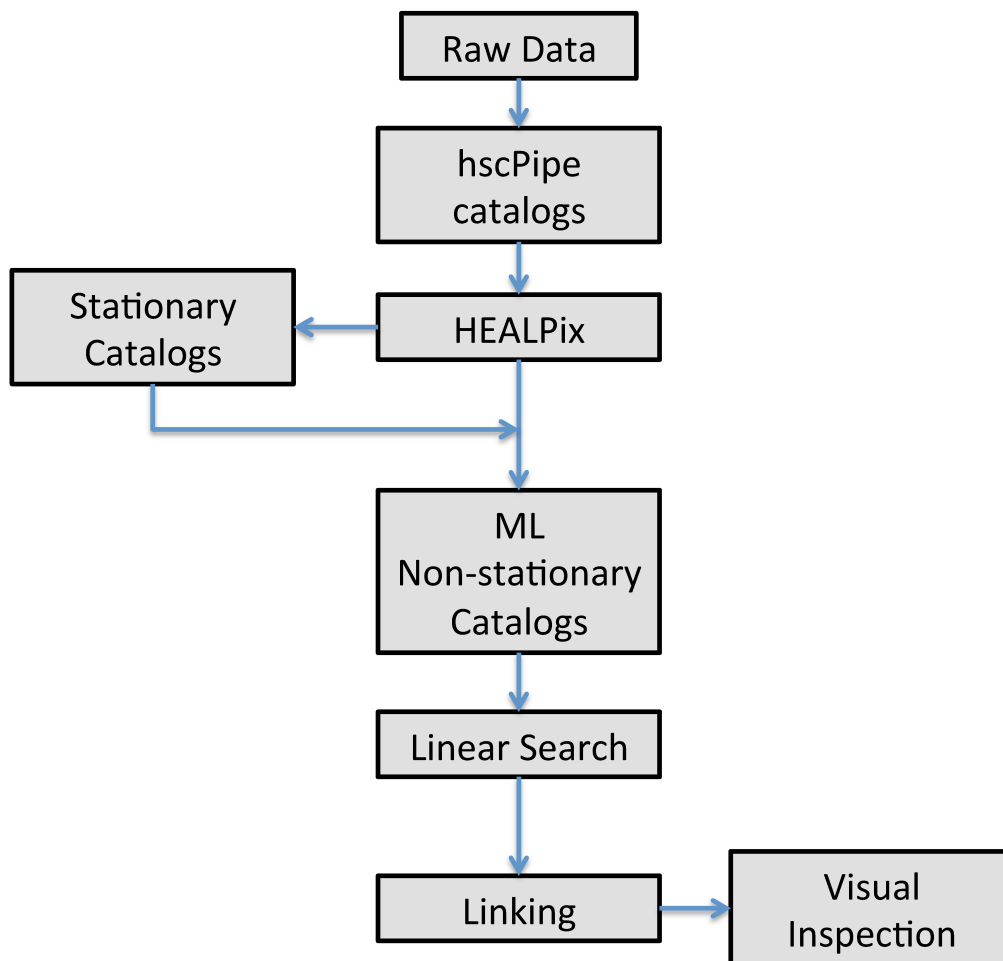


Fig. 4. The flowchart of our pipeline.

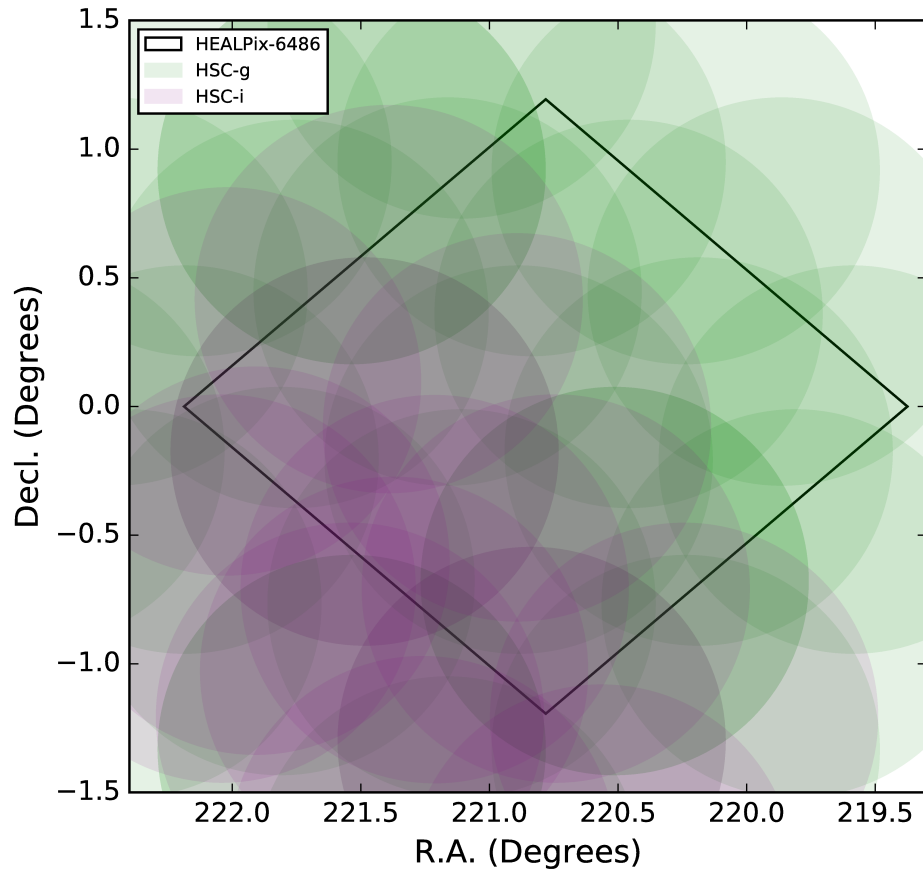


Fig. 5. A comparison of the HSC-SSP dithering pattern and the size of a HEALPix region. The HSC-g (green) and HSC-i (purple) observations are taken in the dark run of May 2015. The size of the HEALPix region was made by the pixelation with $n_{\text{side}} = 32$.

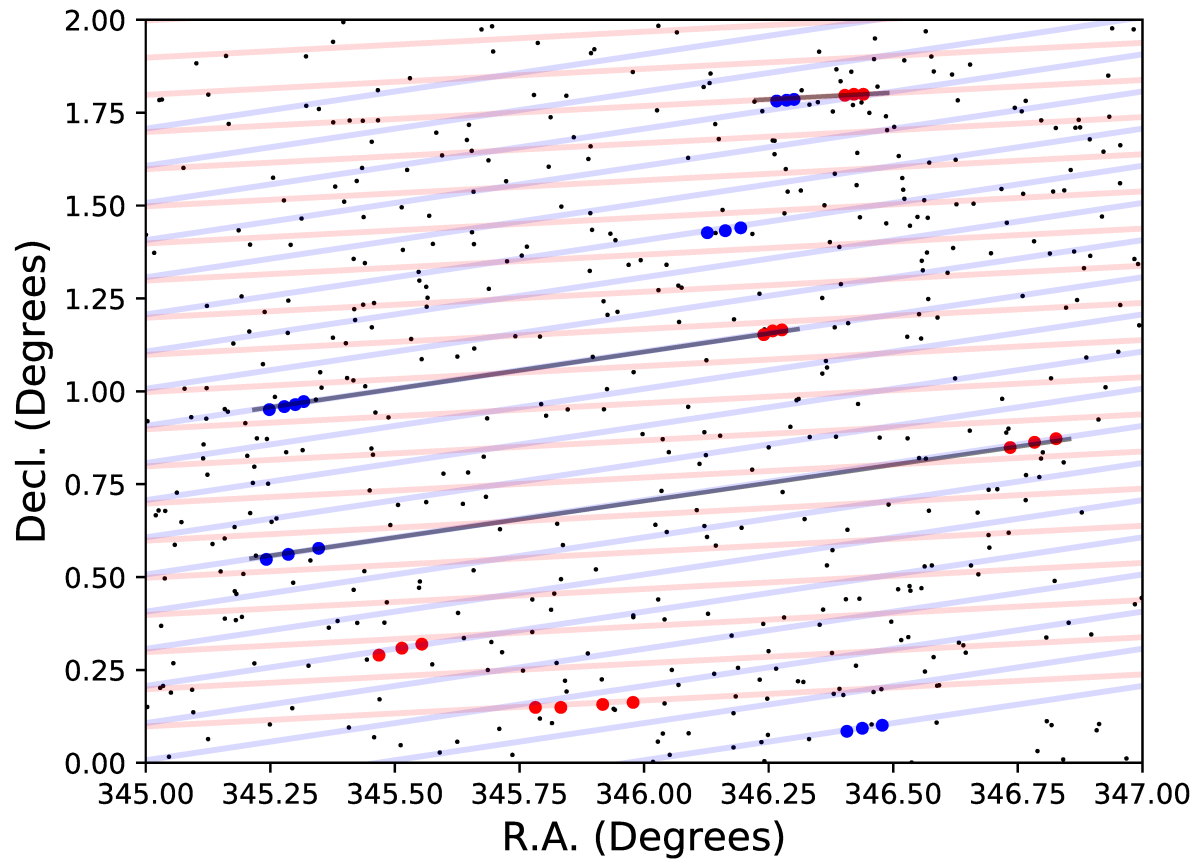


Fig. 6. Illustration of the linear search. The sampling red and blue lines reveal the searches along different directions of motion. The small black dots are objects in the non-stationary catalog, while the large blue and read points are examples of detected tracks in day 1 and day 2. The gray lines indicate the candidates with successful linkages

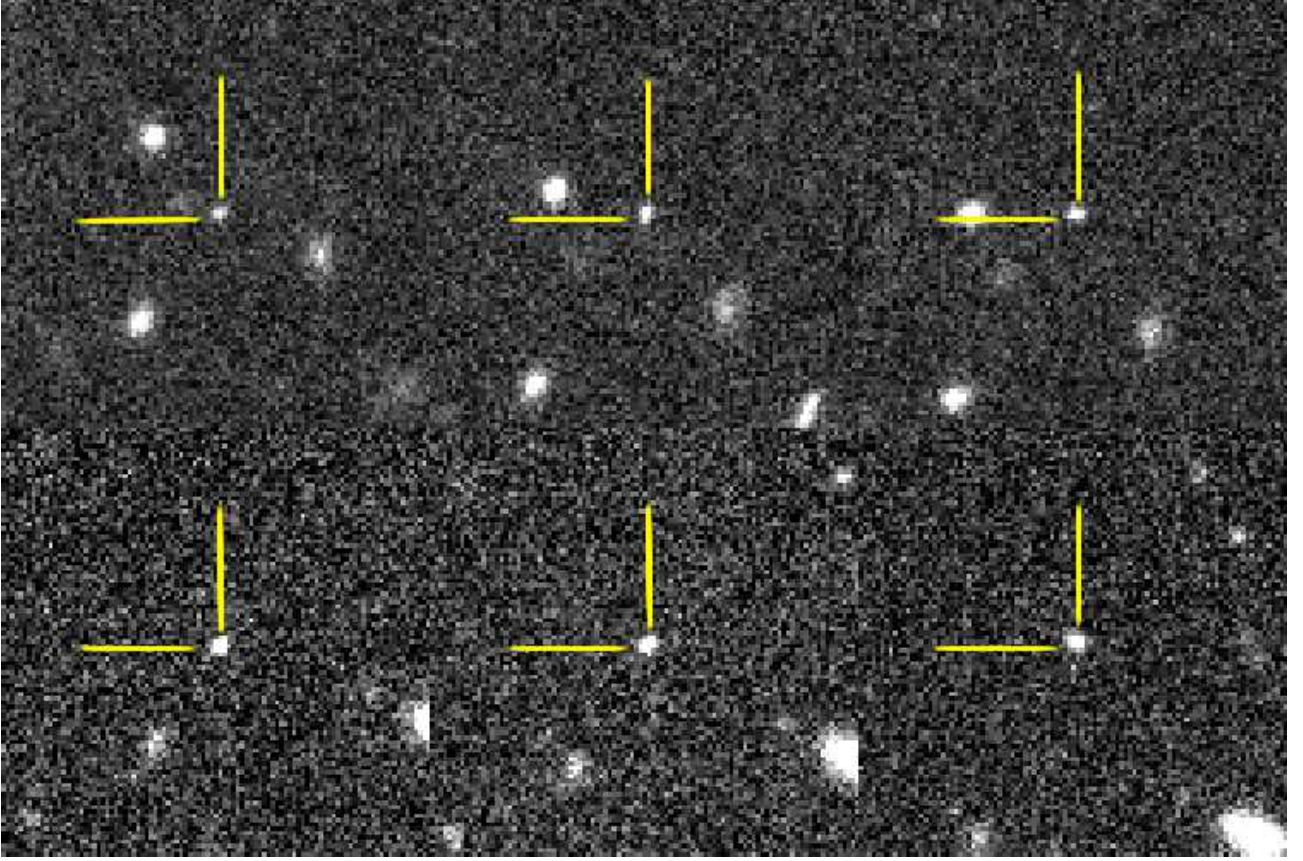


Fig. 7. Postage stamp images of a candidate object(purple lines indicate location of the object), assembled for visual inspection on the Zooniverse platform.

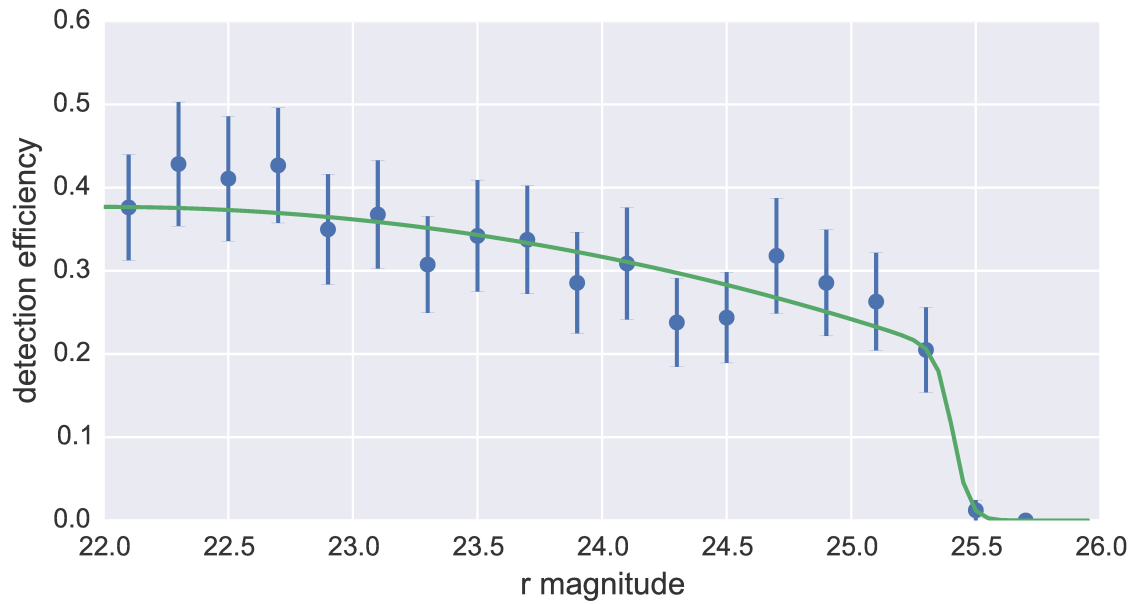


Fig. 8. The detection efficiency for the testing HEALPix, split into bins of magnitude. The best-fit detection efficiency function (see Eq. 1) is illustrated. The original synthetic moving objects have an uniform magnitude distribution with range of 22 - 26.

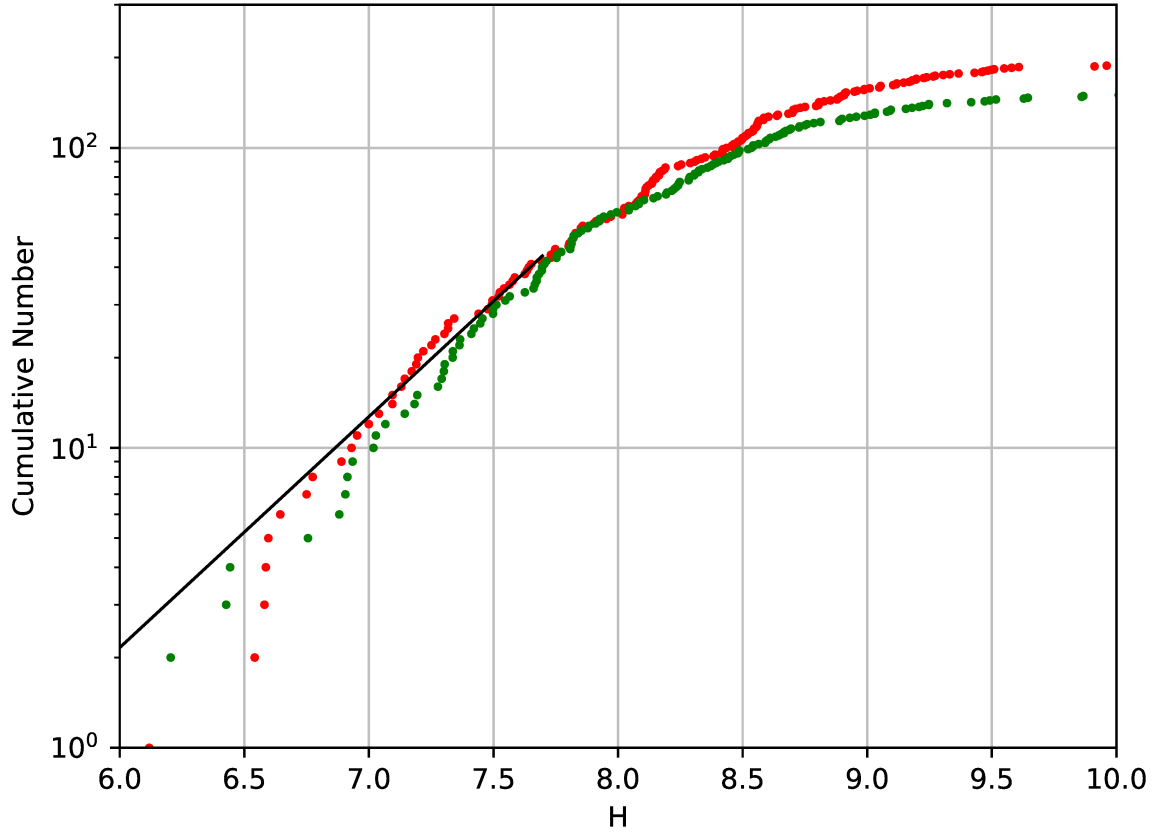


Fig. 9. Absolute magnitude distributions of r -band (red points) and g -band (green points, shifted by a general color term of 0.6) of the hot population KBOs. The two distributions have very similar shapes throughout the entire magnitude range. The black line indicates the best-fit power-law distribution to the total magnitude distribution through $H = 7.7$, which has a power-law slope of .

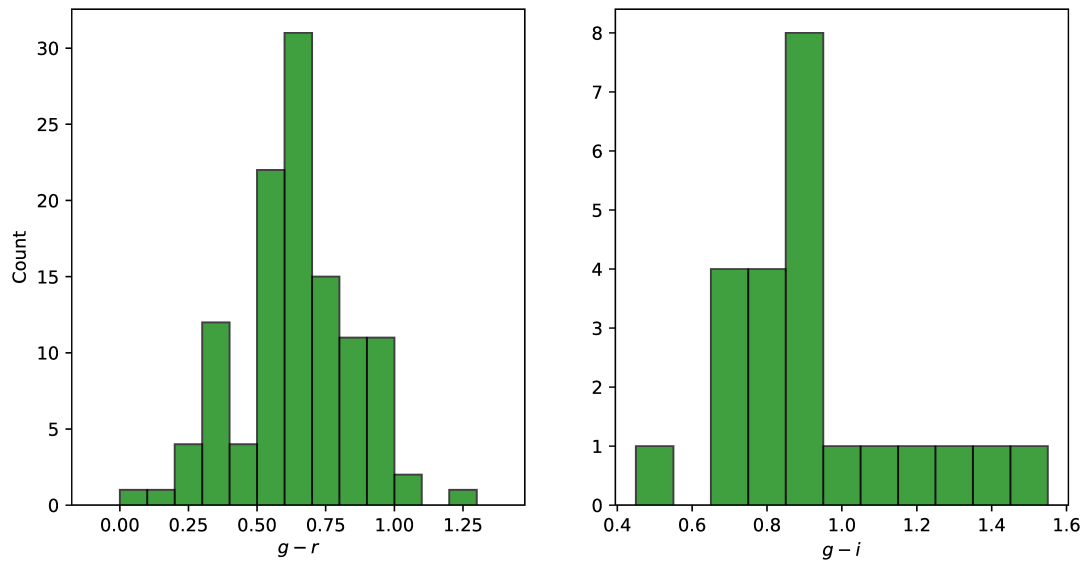


Fig. 10. The $g-r$ and $g-i$ color distribution of HSC-SSP TNOs. The highest bin of $g-i$ consists with the bluer peak of the bimodal color in Wong & Brown (2017)

Table 2. Orbital parameters and photometry of HSC-SSP TNOs in 2014 and 2015.

Name	a (au)	e	i (deg)	g (mag)	r (mag)	i (mag)
20141113-1127.cand001	41.2 \pm 20.9	0.02 \pm 0.58	27.45 \pm 3.2		24.52 \pm 0.08	24.49 \pm 0.21
20141113-1127.cand002	40.3 \pm 20.9	0.02 \pm 0.58	16.70 \pm 0.5		23.73 \pm 0.02	23.55 \pm 0.09
20141113-1127.cand003	48.3 \pm 24.7	0.02 \pm 0.57	19.48 \pm 0.5		24.27 \pm 0.06	23.81 \pm 0.17
20141113-1127.cand004	40.0 \pm 20.2	0.01 \pm 0.58	25.92 \pm 2.8		24.50 \pm 0.12	24.04 \pm 0.10
20141113-1127.cand005	45.8 \pm 23.5	0.02 \pm 0.58	38.23 \pm 9.1	22.23 \pm 0.02		21.87 \pm 0.03
20141113-1127.cand006	40.8 \pm 21.1	0.03 \pm 0.58	19.93 \pm 0.3	24.87 \pm 0.04		23.90 \pm 0.09
20141113-1127.cand007	36.5 \pm 19.0	0.04 \pm 0.57	19.75 \pm 0.5		23.97 \pm 0.00	23.79 \pm 0.08
20141113-1127.cand008	37.1 \pm 19.4	0.03 \pm 0.58	21.52 \pm 0.2		24.03 \pm 0.04	23.79 \pm 0.16
20150312-0330.cand001	45.3 \pm 23.5	0.02 \pm 0.56	16.78 \pm 6.2		24.23 \pm 0.03	23.96 \pm 0.10
20150312-0330.cand002	44.7 \pm 23.2	0.02 \pm 0.56	2.69 \pm 1.0	25.69 \pm 0.07		24.23 \pm 0.02
20150312-0330.cand003	42.9 \pm 22.3	0.02 \pm 0.56	1.01 \pm 0.4	25.46 \pm 0.10		24.19 \pm 0.10
20150312-0330.cand004	44.9 \pm 23.3	0.02 \pm 0.56	0.33 \pm 0.4		24.53 \pm 0.10	24.06 \pm 0.11
20150312-0330.cand005	41.9 \pm 21.8	0.02 \pm 0.56	1.69 \pm 0.7		25.17 \pm 0.19	24.83 \pm 0.22
20150312-0330.cand006	44.5 \pm 23.1	0.02 \pm 0.56	10.80 \pm 3.9		23.92 \pm 0.02	23.94 \pm 0.32
20150312-0330.cand007	44.9 \pm 23.3	0.02 \pm 0.56	0.40 \pm 0.2		25.05 \pm 0.08	24.55 \pm 0.11
20150312-0330.cand008	46.3 \pm 24.0	0.02 \pm 0.56	0.47 \pm 0.5		25.71 \pm 0.02	25.24 \pm 0.09
20150312-0330.cand009	45.9 \pm 23.8	0.02 \pm 0.56	2.92 \pm 1.1		25.07 \pm 0.11	24.79 \pm 0.17
20150312-0330.cand010	44.1 \pm 22.9	0.02 \pm 0.56	1.44 \pm 0.7		24.82 \pm 0.10	24.30 \pm 0.06
20150312-0330.cand011	44.5 \pm 23.2	0.02 \pm 0.58	31.43 \pm 13.4	25.43 \pm 0.11	24.87 \pm 0.05	
20150312-0330.cand012	41.4 \pm 21.7	0.02 \pm 0.58	29.38 \pm 12.5	24.26 \pm 0.06		23.35 \pm 0.06
20150312-0330.cand013	39.6 \pm 20.7	0.02 \pm 0.57	3.99 \pm 1.2	25.50 \pm 0.09		24.07 \pm 0.05
20150312-0330.cand014	47.6 \pm 24.7	0.02 \pm 0.57	25.84 \pm 10.2	24.16 \pm 0.07		23.43 \pm 0.05
20150312-0330.cand015	44.7 \pm 23.2	0.02 \pm 0.56	2.30 \pm 0.2		24.46 \pm 0.06	23.98 \pm 0.15
20150312-0330.cand016	41.3 \pm 21.6	0.02 \pm 0.57	20.52 \pm 8.0		25.46 \pm 0.15	24.74 \pm 0.25
20150312-0330.cand017	46.6 \pm 24.1	0.02 \pm 0.56	2.75 \pm 0.8		25.13 \pm 0.13	24.55 \pm 0.09
20150312-0330.cand018	44.2 \pm 23.0	0.02 \pm 0.56	1.98 \pm 0.4		25.17 \pm 0.21	24.65 \pm 0.04
20150312-0330.cand019	41.5 \pm 22.1	0.02 \pm 0.63	48.99 \pm 31.6		24.43 \pm 0.05	24.06 \pm 0.05
20150312-0330.cand020	41.4 \pm 21.7	0.02 \pm 0.58	29.37 \pm 12.4		23.59 \pm 0.04	23.44 \pm 0.03
20150312-0330.cand021	46.1 \pm 23.9	0.02 \pm 0.56	1.81 \pm 0.6	24.50 \pm 0.06		23.45 \pm 0.03
20150312-0330.cand022	41.2 \pm 21.5	0.02 \pm 0.57	17.88 \pm 6.8	24.83 \pm 0.07		23.89 \pm 0.11
20150312-0330.cand023	54.7 \pm 28.1	0.02 \pm 0.55	6.42 \pm 2.1	25.16 \pm 0.14		23.78 \pm 0.04

Table 2. (Continued)

20150312-0330.cand024	41.9±21.9	0.02±0.56	1.17±0.3	24.89±0.12		23.63±0.10
20150312-0330.cand025	43.9±23.0	0.02±0.59	38.57±18.5	25.41±0.24		24.62±0.25
20150312-0330.cand026	44.5±23.1	0.02±0.56	1.56±0.2	24.85±0.18		23.38±0.06
20150312-0330.cand027	48.6±25.1	0.02±0.56	1.50±0.1	23.77±0.05		22.52±0.15
20150312-0330.cand028	42.0±21.9	0.02±0.56	1.27±0.2	24.23±0.23	23.02±0.02	
20150312-0330.cand029	44.5±23.1	0.02±0.56	7.61±2.7			24.11±0.09
20150312-0330.cand030	50.2±25.9	0.02±0.55	1.76±0.6		24.93±0.11	24.86±0.12
20150312-0330.cand031	43.8±22.8	0.02±0.56	2.14±0.4		23.41±0.07	22.90±0.01
20150312-0330.cand032	54.2±27.8	0.02±0.55	1.70±0.8		25.36±0.16	24.69±0.07
20150312-0330.cand033	42.2±22.0	0.02±0.56	2.91±1.1		24.12±0.10	23.74±0.10
20150312-0330.cand034	42.3±22.0	0.02±0.56	4.76±1.7		24.69±0.12	24.22±0.07
20150312-0330.cand035	46.6±24.1	0.02±0.56	4.96±1.7		23.15±0.11	22.68±0.05
20150312-0330.cand036	43.5±22.6	0.02±0.56	2.60±0.9		25.14±0.14	24.64±0.09
20150312-0330.cand037	43.1±22.5	0.02±0.56	3.62±1.3		24.00±0.03	23.57±0.04
20150312-0330.cand038	47.4±24.5	0.02±0.56	1.00±0.0		25.32±0.22	24.81±0.18
20150312-0330.cand039	47.6±24.6	0.02±0.56	4.01±1.4		24.65±0.07	24.32±0.05
20150312-0330.cand040	43.5±22.6	0.02±0.56	1.32±0.5		25.12±0.12	24.51±0.11
20150312-0330.cand041	42.2±22.0	0.02±0.56	1.49±0.3		25.08±0.08	24.79±0.16
20150312-0330.cand042	36.0±19.0	0.03±0.58	24.77±10.4		25.29±0.03	24.90±0.03
20150312-0330.cand043	47.8±24.8	0.02±0.57	32.71±13.9		25.16±0.08	24.83±0.04
20150312-0330.cand044	44.5±23.1	0.02±0.56	0.85±0.2		25.28±0.07	24.90±0.12
20150312-0330.cand045	47.8±24.7	0.02±0.56	1.18±0.1		24.83±0.07	24.43±0.04
20150312-0330.cand046	46.1±23.9	0.02±0.56	1.70±0.6		24.64±0.12	24.37±0.07
20150312-0330.cand047	48.2±24.9	0.02±0.56	1.05±0.4		23.45±0.03	22.96±0.03
20150312-0330.cand048	53.1±27.3	0.02±0.55	8.49±3.0		24.96±0.04	24.81±0.12
20150312-0330.cand049	43.6±22.7	0.02±0.56	1.20±0.3		24.78±0.03	24.34±0.07
20150312-0330.cand050	42.5±22.2	0.02±0.56	1.26±0.4		25.04±0.03	24.46±0.16
20150312-0330.cand051	45.5±23.6	0.02±0.56	1.22±0.2		25.14±0.04	24.93±0.06
20150312-0330.cand052	38.3±20.1	0.03±0.57	6.72±2.5		25.17±0.15	24.62±0.17
20150312-0330.cand053	42.4±22.1	0.02±0.56	1.24±0.2		25.02±0.16	24.51±0.08
20150312-0330.cand054	43.4±22.6	0.02±0.56	2.25±0.8		25.37±0.06	24.54±0.06
20150312-0330.cand055	46.7±24.2	0.02±0.56	3.22±1.2		23.72±0.05	23.56±0.04
20150312-0330.cand056	42.3±22.2	0.02±0.59	38.91±19.1		24.67±0.08	24.31±0.08

Table 2. (Continued)

20150312-0330.cand057	56.0±28.8	0.02±0.55	20.77±7.5	25.73±0.14		24.44±0.07
20150312-0330.cand058	40.2±21.0	0.02±0.58	24.49±9.9	24.47±0.08		23.62±0.07
20150312-0330.cand059	37.4±19.8	0.03±0.60	35.30±17.0	24.74±0.13		23.83±0.07
20150312-0330.cand060	45.4±23.6	0.02±0.56	22.11±8.5	25.58±0.05		25.12±0.37
20150312-0330.cand061	40.4±21.1	0.02±0.57	1.68±0.1	25.10±0.08		24.50±0.12
20150312-0330.cand062	43.4±22.6	0.02±0.56	1.45±0.3	25.19±0.19	24.37±0.11	
20150312-0330.cand063	38.8±20.4	0.03±0.57	14.87±5.7	25.64±0.25	25.05±0.08	
20150312-0330.cand064	42.9±22.3	0.02±0.56	2.19±0.8		24.87±0.07	24.48±0.08
20150312-0330.cand065	44.1±22.9	0.02±0.56	5.26±1.8		25.10±0.17	24.56±0.07
20150312-0330.cand066	37.4±19.8	0.03±0.60	35.20±16.9		24.04±0.04	23.86±0.03
20150312-0330.cand067	41.8±21.8	0.02±0.56	7.25±2.5		24.95±0.17	24.81±0.03
20150312-0330.cand068	46.2±23.9	0.02±0.56	2.82±1.0		24.14±0.05	23.84±0.03
20150312-0330.cand069	45.8±23.7	0.02±0.56	9.26±3.3		25.03±0.11	24.51±0.03
20150312-0330.cand070	44.2±23.0	0.02±0.56	1.10±0.3		25.25±0.23	24.98±0.22
20150312-0330.cand071	36.9±19.4	0.03±0.57	8.10±3.1		24.13±0.09	23.99±0.03
20150312-0330.cand072	43.8±22.8	0.02±0.56	0.85±0.2		25.32±0.02	24.91±0.14
20150312-0330.cand073	44.8±23.2	0.02±0.56	1.03±0.5		24.92±0.11	24.52±0.10
20150312-0330.cand074	44.3±23.0	0.02±0.56	1.66±0.7		25.31±0.12	24.40±0.82
20150312-0330.cand075	50.0±25.8	0.02±0.56	24.61±9.5		25.20±0.12	25.13±0.16
20150312-0330.cand076	47.9±24.8	0.02±0.56	1.55±0.6		24.29±0.06	23.97±0.13
20150312-0330.cand077	49.7±25.6	0.02±0.55	4.53±1.7		25.22±0.15	25.03±0.08
20150312-0330.cand078	44.1±22.9	0.02±0.56	1.90±0.2		24.77±0.08	24.59±0.17
20150312-0330.cand079	27.8±2.1	0.65±0.03	52.05±21.2	25.27±0.08		24.41±0.16
20150312-0330.cand080	41.3±21.6	0.02±0.58	28.05±11.7		25.06±0.06	24.56±0.06
20150312-0330.cand081	40.0±20.9	0.03±0.57	4.66±1.5	25.10±0.07	24.65±0.06	
20150312-0330.cand082	49.3±25.4	0.02±0.55	3.24±0.9	25.56±0.10		24.32±0.09
20150312-0330.cand083	41.9±21.9	0.02±0.56	2.26±0.4	25.27±0.09		24.01±0.03
20150312-0330.cand084	42.5±22.1	0.02±0.56	2.90±0.7		24.73±0.10	24.23±0.05
20150312-0330.cand085	45.7±23.7	0.02±0.56	2.56±0.6		23.41±0.01	23.08±0.04
20150312-0330.cand086	40.6±21.2	0.02±0.57	6.64±2.2		25.42±0.04	24.99±0.13
20150312-0330.cand087	40.5±21.2	0.02±0.57	11.23±4.1		25.28±0.06	24.78±0.16
20150312-0330.cand088	44.8±23.3	0.02±0.56	0.54±0.2	24.64±0.09	23.68±0.07	
20150312-0330.cand089	44.1±22.9	0.02±0.56	1.86±0.8		24.68±0.04	24.31±0.03

Table 2. (Continued)

20150312-0330.cand090	42.1±22.0	0.02±0.58	27.91±11.7		25.26±0.12	24.68±0.11
20150312-0330.cand091	45.6±23.6	0.02±0.56	0.90±0.5		24.11±0.05	23.65±0.07
20150312-0330.cand092	42.0±21.9	0.02±0.56	8.03±3.0		25.50±0.01	25.17±0.12
20150312-0330.cand093	42.5±22.1	0.02±0.59	25.94±12.2	25.74±0.08	25.27±0.19	
20150312-0330.cand094	34.0±17.9	0.03±0.59	16.87±1.2		23.69±0.07	23.65±0.25
20150312-0330.cand095	36.6±19.1	0.03±0.59	22.73±3.2	25.32±0.10	24.67±0.11	
20150312-0330.cand096	22.1±11.8	0.02±0.59	164.60±0.2	25.40±0.09	24.41±0.47	
20150312-0330.cand097	43.3±22.3	0.02±0.58	15.93±0.1	24.56±0.06	24.21±0.03	
20150312-0330.cand098	42.7±22.0	0.02±0.58	20.06±1.0	25.06±0.08	24.46±0.23	
20150312-0330.cand099	28.4±0.4	0.93±0.70	12.32±3.6	24.36±0.10	24.92±0.04	
20150312-0330.cand100	22.9±12.8	0.04±0.64	14.12±0.7	23.10±0.04		21.68±0.04
20150312-0330.cand101	42.4±21.9	0.02±0.58	25.51±3.7			24.17±0.08
20150511-0525.cand001	24.1±13.3	0.04±0.48	121.98±10.9	25.12±0.06	24.36±0.08	
20150511-0525.cand002	37.4±19.7	0.03±0.59	26.51±12.0	24.40±0.10	23.75±0.07	
20150511-0525.cand003	45.7±23.6	0.02±0.57	12.25±0.9	25.47±0.06	24.79±0.09	
20150511-0525.cand004	45.1±23.5	0.02±0.60	36.19±18.9	24.19±0.08	23.60±0.05	
20150511-0525.cand005	35.4±18.8	0.03±0.60	25.12±10.7	24.80±0.39	24.02±0.11	
20150511-0525.cand006	37.8±19.8	0.03±0.58	12.30±0.6	24.61±0.08	23.56±0.03	
20150511-0525.cand007	44.6±23.1	0.02±0.57	15.97±3.3	25.33±0.16	24.45±0.06	
20150511-0525.cand008	41.9±21.9	0.02±0.59	28.99±12.7	25.16±0.12	24.53±0.13	
20150511-0525.cand009	26.9±14.7	0.04±0.62	25.19±7.1	24.66±0.08	24.01±0.07	
20150511-0525.cand010	38.0±19.9	0.03±0.58	17.00±4.7	25.45±0.06	24.63±0.13	
20150511-0525.cand011	39.5±20.7	0.03±0.58	22.50±8.0	25.30±0.01	24.69±0.14	
20150511-0525.cand012	33.6±17.8	0.03±0.59	18.78±6.2	24.40±0.15	23.51±0.04	
20150511-0525.cand013	41.1±21.4	0.02±0.57	13.81±0.5	25.22±0.15	24.41±0.06	
20150511-0525.cand014	36.7±19.3	0.03±0.58	12.07±0.1	23.88±0.13	23.56±0.04	
20150511-0525.cand015	39.6±20.7	0.03±0.57	14.82±0.5	24.10±0.04	23.56±0.05	
20150511-0525.cand016	47.1±24.3	0.02±0.56	23.79±4.0	24.22±0.09		23.55±0.04
20150511-0525.cand017	40.2±20.9	0.03±0.57	15.09±0.3	24.30±0.05		23.14±0.02
20150511-0525.cand018	35.2±18.6	0.03±0.58	15.18±0.1	22.79±0.10		21.25±0.05
20150511-0525.cand019	41.8±21.8	0.02±0.57	21.06±5.7	24.00±0.08	23.25±0.05	
20150511-0525.cand020	33.8±18.0	0.03±0.60	24.35±9.3	24.39±0.04		23.45±0.08
20150511-0525.cand021	35.8±18.9	0.03±0.58	17.94±2.1	25.04±0.13		24.31±0.16

Table 2. (Continued)

20150511-0525.cand022	31.6±16.9	0.03±0.59	18.05±4.3	24.86±0.07	24.01±0.10
20150511-0525.cand023	37.8±19.8	0.03±0.57	14.95±0.1	24.63±0.09	23.49±0.04
20150511-0525.cand024	40.2±21.0	0.02±0.57	14.41±0.1	24.18±0.13	23.41±0.06
20150511-0525.cand025	25.3±13.7	0.03±0.50	160.92±1.1	24.28±0.05	23.58±0.07
20150511-0525.cand026	49.7±25.6	0.02±0.57	19.76±5.1	25.39±0.13	24.50±0.04
20150511-0525.cand027	40.4±21.1	0.02±0.59	28.69±11.5	23.70±0.08	22.80±0.03
20150511-0525.cand028	35.6±18.8	0.03±0.59	23.34±7.9	24.55±0.12	23.78±0.04
20151005-1020.cand001	46.9±24.3	0.02±0.56	6.92±0.4	25.01±0.09	24.30±0.07
20151005-1020.cand002	33.9±18.0	0.03±0.58	9.82±2.6	24.95±0.20	24.57±0.02
20151005-1020.cand003	38.9±20.4	0.02±0.57	6.71±0.4	24.41±0.02	23.76±0.03
20151005-1020.cand004	41.8±21.8	0.02±0.57	11.49±2.8	25.17±0.01	24.88±0.15
20151005-1020.cand005	41.9±21.8	0.02±0.57	12.65±3.8	25.15±0.16	24.17±0.07
20151005-1020.cand006	29.6±16.1	0.03±0.49	135.76±9.1	24.60±0.05	24.07±0.01
20151005-1020.cand007	43.7±22.8	0.02±0.56	12.94±3.6	24.71±0.07	23.78±0.07
20151005-1020.cand008	51.1±26.4	0.02±0.56	17.90±5.7	25.42±0.06	24.80±0.07
20151005-1020.cand009	48.2±24.9	0.02±0.56	6.52±0.8	25.10±0.04	24.83±0.18
20151005-1020.cand010	45.9±23.8	0.02±0.56	5.30±0.4	25.27±0.13	24.39±0.13
20151005-1020.cand011	46.6±24.2	0.02±0.56	5.49±0.3	24.60±0.40	23.76±0.06
20151005-1020.cand012	41.7±21.8	0.02±0.57	27.20±10.4	25.40±0.16	25.10±0.08
20151005-1020.cand013	40.4±21.2	0.03±0.57	21.14±7.4	25.16±0.14	24.46±0.09
20151005-1020.cand014	51.8±26.7	0.02±0.55	16.30±5.0	25.10±0.08	24.45±0.07
20151005-1020.cand015	35.6±18.8	0.03±0.58	20.59±7.5	24.38±0.02	23.76±0.24
20151005-1020.cand016	42.7±22.3	0.03±0.56	9.39±1.4	24.40±0.07	23.77±0.18
20151005-1020.cand017	46.8±24.2	0.02±0.56	8.56±0.7	24.79±0.10	23.81±0.05
20151005-1020.cand018	43.2±22.6	0.02±0.58	32.97±13.8	24.51±0.08	23.70±0.02
20151005-1020.cand019	46.5±24.1	0.02±0.56	9.72±1.6	24.44±0.08	23.83±0.05
20151005-1020.cand020	33.7±17.9	0.03±0.58	6.37±0.1	24.14±0.04	23.23±0.03
20151005-1020.cand021	35.1±18.6	0.03±0.58	16.29±5.3	24.96±0.13	24.44±0.13
20151005-1020.cand022	31.2±16.7	0.03±0.59	6.99±1.5	24.96±0.13	23.97±0.04
20151005-1020.cand023	46.8±24.2	0.02±0.56	5.04±0.1	24.73±0.27	23.66±0.09
20151005-1020.cand024	43.2±22.5	0.02±0.56	5.66±0.3	24.71±0.08	23.89±0.02
20151005-1020.cand025	35.3±18.7	0.03±0.58	10.54±3.0	24.56±0.11	23.93±0.05
20151005-1020.cand026	20.6±11.6	0.05±0.49	142.97±6.9	24.56±0.07	23.94±0.07

Table 2. (Continued)

20151005-1020.cand027	46.6±24.2	0.02±0.56	9.84±2.8	23.59±0.07	23.09±0.06
20151005-1020.cand028	38.9±20.5	0.03±0.58	31.08±13.3	24.77±0.13	24.44±0.08
20151005-1020.cand029	39.6±20.8	0.03±0.57	20.84±7.3	23.29±0.07	22.70±0.02
20151005-1020.cand030	48.4±25.0	0.02±0.56	24.62±8.8	25.40±0.09	25.17±0.04
20151005-1020.cand031	44.2±23.0	0.02±0.56	6.89±0.5	25.28±0.18	25.05±0.39
20151005-1020.cand032	45.0±23.4	0.02±0.56	17.39±5.8	25.18±0.23	24.55±0.19
20151005-1020.cand033	41.8±22.6	0.02±0.66	53.20±39.6	23.93±0.69	22.63±0.07
20151005-1020.cand034	47.1±24.4	0.02±0.56	6.27±0.0	24.56±0.12	24.08±0.05
20151005-1020.cand035	31.9±17.0	0.03±0.59	11.34±2.9	24.61±0.04	24.05±0.11
20151005-1020.cand036	39.0±20.5	0.03±0.57	7.14±0.7	24.39±0.13	23.78±0.06
20151005-1020.cand037	46.2±24.0	0.02±0.57	26.40±9.9	25.19±0.15	25.05±0.14
20151005-1020.cand038	32.3±17.3	0.03±0.59	17.44±6.0	25.35±0.19	24.49±0.04
20151005-1020.cand039	45.7±23.7	0.02±0.56	11.25±2.7	25.36±0.17	25.00±0.61
20151005-1020.cand040	50.0±25.8	0.02±0.57	32.14±12.4	25.25±0.12	24.73±0.07
20151005-1020.cand041	44.4±23.1	0.02±0.56	7.92±0.0	24.76±0.06	24.40±0.09
20151005-1020.cand042	44.4±23.1	0.02±0.56	7.95±0.0	24.60±0.10	23.87±0.04
20151005-1020.cand043	38.1±20.0	0.03±0.57	10.95±1.6	23.92±0.16	22.98±0.07
20151005-1020.cand044	41.5±21.7	0.03±0.56	10.66±1.8	25.28±0.15	24.26±0.09
20151005-1020.cand045	35.4±18.7	0.03±0.58	9.98±1.6	24.44±0.02	23.84±0.09
20151005-1020.cand046	45.2±23.5	0.02±0.56	8.27±0.3	24.98±0.21	24.57±0.08
20151005-1020.cand047	55.8±28.6	0.02±0.55	22.77±7.4	25.02±0.13	24.36±0.03
20151005-1020.cand048	57.2±29.4	0.02±0.56	35.73±14.3	25.49±0.09	24.78±0.12
20151005-1020.cand049	35.4±18.7	0.03±0.58	10.74±2.1	24.19±0.04	23.60±0.09
20151005-1020.cand050	38.9±20.4	0.03±0.57	9.84±1.1	25.28±0.10	24.64±0.06
20151005-1020.cand051	35.5±18.8	0.03±0.57	8.68±0.9	25.13±0.13	24.23±0.05
20151005-1020.cand052	43.2±22.5	0.02±0.56	11.54±2.9	24.94±0.10	24.31±0.16
20151005-1020.cand053	37.3±19.6	0.03±0.57	7.18±0.2	24.58±0.10	24.01±0.07
20151005-1020.cand054	35.5±18.8	0.03±0.58	19.15±6.3	25.32±0.08	24.42±0.13
20151005-1020.cand055	45.7±23.8	0.02±0.57	32.60±13.2	24.51±0.11	23.73±0.17
20151005-1020.cand056	34.7±18.4	0.03±0.58	10.44±2.0	24.10±0.08	23.55±0.05
20151005-1020.cand057	40.1±21.0	0.02±0.58	25.02±9.3	25.38±0.16	25.36±0.27
20151005-1020.cand058	39.4±20.6	0.02±0.58	29.40±9.0	25.32±0.11	24.58±0.11
20151005-1020.cand059	42.7±22.2	0.02±0.56	14.36±0.4	23.51±0.03	22.75±0.02

Table 2. (Continued)

20151005-1020.cand060	40.8±21.3	0.02±0.57	14.73±1.3	23.91±0.04	23.07±0.01
20151005-1020.cand061	38.7±20.3	0.03±0.57	19.13±3.4	24.95±0.04	24.26±0.08
20151005-1020.cand062	47.0±24.3	0.02±0.56	15.62±0.0	24.99±0.07	24.31±0.08
20151005-1020.cand063	45.2±23.4	0.02±0.56	17.29±1.8	24.15±0.08	23.18±0.04
20151005-1020.cand064	33.9±18.0	0.03±0.59	29.57±8.8	25.21±0.13	24.67±0.08
20151005-1020.cand065	55.1±28.2	0.02±0.55	15.03±0.0	25.40±0.11	24.78±0.03
20151005-1020.cand066	47.0±24.3	0.02±0.56	14.60±0.0	25.22±0.06	24.69±0.08
20151005-1020.cand067	41.4±21.6	0.02±0.58	29.07±9.8	24.96±0.12	24.44±0.07
20151005-1020.cand068	41.1±21.6	0.03±0.60	42.99±21.5	25.34±0.13	24.83±0.14
20151005-1020.cand069	43.6±22.7	0.02±0.58	33.98±13.0	25.44±0.11	25.06±0.05
20151005-1020.cand070	38.8±20.3	0.02±0.57	15.74±0.5	25.36±0.16	24.99±0.14
20151005-1020.cand071	38.6±20.2	0.03±0.57	16.08±1.6	24.58±0.08	23.80±0.13
20151005-1020.cand072	34.8±18.4	0.03±0.58	14.74±0.4	24.08±0.20	23.31±0.07
20151005-1020.cand073	43.3±22.5	0.02±0.57	21.56±4.7	25.06±0.12	24.41±0.04
20151005-1020.cand074	70.0±35.5	0.01±0.54	15.11±0.3	25.17±0.11	24.48±0.09
20151005-1020.cand075	48.1±24.9	0.02±0.58	39.92±14.7	24.63±0.12	23.79±0.06
20151005-1020.cand076	39.1±20.4	0.03±0.57	14.27±0.1	25.36±0.15	25.02±0.15
20151005-1020.cand077	43.1±22.3	0.02±0.56	14.69±0.1	25.61±0.16	24.93±0.10
20151005-1020.cand078	30.2±16.2	0.03±0.59	14.98±0.3	25.65±0.22	25.02±0.09
20151005-1020.cand079	31.7±16.9	0.03±0.59	18.37±2.3	25.06±0.10	24.12±0.04
20151005-1020.cand080	33.8±17.9	0.03±0.59	23.50±6.8	23.44±0.02	22.92±0.03
20151005-1020.cand081	39.5±20.6	0.03±0.57	17.19±1.9	23.43±0.03	22.84±0.03
20151005-1020.cand082	41.5±21.6	0.02±0.57	16.86±1.6	24.56±0.02	23.83±0.03
20151005-1020.cand083	38.2±20.0	0.03±0.57	18.99±1.9	25.28±0.13	24.81±0.12
20151005-1020.cand084	39.7±20.7	0.02±0.57	27.22±6.4	24.31±0.05	23.68±0.03
20151005-1020.cand085	20.7±11.5	0.05±0.50	156.85±2.0	25.22±0.11	24.50±0.22
20151005-1020.cand086	39.9±20.8	0.02±0.57	17.57±0.9	24.56±0.05	23.94±0.09
20151005-1020.cand087	48.4±25.0	0.02±0.56	18.40±1.4	24.83±0.27	24.46±0.14
20151005-1020.cand088	39.6±20.7	0.02±0.57	20.61±2.2	23.35±0.04	22.46±0.04
20151005-1020.cand089	45.3±23.4	0.02±0.56	16.99±1.2	25.56±0.15	24.89±0.08
20151005-1020.cand090	52.4±26.9	0.02±0.56	17.49±1.2	24.97±0.14	24.60±0.10
20151005-1020.cand091	46.9±24.2	0.02±0.57	23.63±5.9	24.99±0.10	24.48±0.06
20151005-1020.cand092	40.1±20.9	0.03±0.58	26.83±8.3	25.25±0.07	24.67±0.10

Table 2. (Continued)

20151005-1020.cand093	41.1 ± 21.4	0.02 ± 0.58	27.66 ± 8.7	24.81 ± 0.14	24.11 ± 0.11
20151005-1020.cand094	39.9 ± 20.8	0.03 ± 0.59	10.95 ± 4.5	24.78 ± 0.17	24.10 ± 0.07
